Response of the Neutral Thermosphere at F-Layer Heights to Interaction of a Global Wind with Anomalies of Ionization

ROBERT E. DICKINSON, R. G. ROBLE AND E. C. RIDLEY

National Center for Atmospheric Research,[1] Boulder, Colo.

(Manuscript received 4 May 1971)

ABSTRACT

Departures from a mean global-scale ionization distribution are commonly found in the ionospheric F region. Global-scale winds experience an acceleration where the ion drag is locally less than its global-scale smooth value and, they likewise, experience a deceleration where the ion drag is locally greater. Thus, a perturbation in the horizontal flow is set up in response to this ion-drag momentum source.

A two-dimensional, steady-state dynamic model of the neutral thermosphere, incorporating thermal conduction, viscosity and ion drag, is used to calculate the temperature perturbation and circulation pattern caused by these ion-drag anomalies. The forcing is given by a momentum source which depends on the interaction of a basic-state neutral wind with the anomaly. For horizontal-scale anomalies of a few hundred kilometers, such as the electron density depression within the stable auroral red arc, the momentum source due to perturbation ion drag is almost completely balanced by a perturbation pressure force. The perturbation temperature and circulation responses are, therefore, negligibly small. For horizontal-scale anomalies of the order of a few thousand kilometers, such as the day-night electron density variation at sunset, the force exerted by the perturbation pressure is not able to cancel the addition of momentum by the ion-drag anomaly.Thus, such a momentum source produces a significant perturbation in the horizontal velocity, vertical motion, and temperature field.

1. Introduction

Global-scale asymmetries in the distribution of pressure at a given level in the thermosphere drive horizontal wind systems with amplitudes up to several hundred meters per second (Kohl and King, 1967; Geisler, 1967). A given distribution of these pressure forces is balanced in the equations of motion by inertial, ion drag, Coriolis and viscous forces. Above about 150 km, the ion drag and viscous forces essentially control the amplitudes of the wind systems calculated in this fashion. Indeed, for the large vertical scales of the order of several hundred kilometers, which are implicit in the above-referenced calculations, the wind amplitudes are determined to a first approximation below the F2 peak by the balance between ion drag and pressure forces.

The ion drag on the neutral motions at F2 layer heights is directly proportional to the ion and, hence, to the electron concentration. Various anomalies are observed in F2 layer ionization. We use the term ionization anomaly to denote a departure from the global-scale ionization distribution. Global-scale winds forced by global-scale pressure gradients should experience acceleration where the ion drag is locally less than its global-scale smooth value and, likewise, they should experience deceleration where the ion drag is locally greater. A perturbation of the horizontal flow is set up and vertical velocities must occur as well. The resulting distribution of adiabatic warming and cooling should produce perturbation temperatures and, consequently, pressures whose horizontal gradients partially balance the perturbation ion drag. Hence, the strength of the anomaly in the winds should be less than that which would be inferred from the ion-drag anomaly alone.

Our interest in this problem derives originally from consideration of the possible consequences of the large depression in electron concentration accompanying stable auroral red arcs (Roble *et al.*, 1970), which occur in mid-latitudes during geomagnetic storms. The ionization within the red arc is depressed by as much as an order of magnitude over a distance of roughly 100 km in the horizontal. Some examples of this phenomenon which we considered indicated that the perturbation in the ion drag, if there were no perturbation in the pressure distribution, might accelerate the horizontal winds from around 200 m sec^{-1} at the edge of the anomaly to around 300 m sec^{-1} at the center of the anomaly. At the center of the anomaly, the wind amplitudes are determined largely by the balance between pressure forces and viscous drag; outside the anomaly, ion drag is significant in determining the amplitudes. A 100 m sec^{-1} horizontal variation of wind implies, by continuity, vertical velocities as large as 50 m sec^{-1}.

[1] The National Center for Atmospheric Research is sponsored by the National Science Foundation.

The flow is upward on the upstream side, and downward on the downstream side of the anomaly's center. Steady vertical motion of this magnitude is quite unlikely because of the large adiabatic heating that would result.

The purpose of this study is to examine the circulations that are forced by anomalies in the ionization, in terms of a self-consistent dynamic model in which the resulting back-pressure force is included in the calculation. Examination of the various balances in the equations of the model shows, for a sufficiently small horizontal anomaly in ion drag, that the resulting momentum source is almost completely balanced by the perturbation pressures. The circulation is then negligibly small. On the other hand, for a sufficiently large horizontal anomaly in ion drag, the force exerted by the perturbation pressure will not be able to cancel the addition of momentum by the ion drag anomaly. This addition of momentum must then produce significant perturbations in the horizontal velocity, the vertical motion, and the temperature field. Because of the large number of possible applications of the theory presented in this study, it does not seem worthwhile to model any of the particular physical occurrences in detail. Rather, we seek to provide a general description of the dependence of the neutral atmosphere's response on parameters characterizing the assumed perturbation momentum source.

Numerical integrations of the dynamic model provide more precise information concerning the neutral circulation that ensues from an anomaly in the ion drag. The circulation depends on the horizontal scale of the anomaly, on the magnitude and vertical structure of the perturbation and global-scale ionization, and on the global-scale wind. While our analysis is described in terms of the perturbation momentum source provided by global winds experiencing local variations in ion drag, many of our conclusions are equally valid for other steady momentum sources at F2 layer heights. In particular, we gain insight into the neutral circulations produced by local components of steady plasma drifts accelerating the neutral gas through ion drag.

2. Governing equations

We assume a global-scale wind system and a smooth global-scale distribution of ionization which defines the basic-state ion drag exerted on this wind. The horizontal coordinate x is chosen orthogonal to the orientation of an assumed local anomaly in ionization which results in a perturbation ion drag coefficient $\lambda(x,z)$. The vertical coordinate z is the log of inverse pressure. The basic-state ion drag $D(z)$ in the x direction depends on z according to

$$D(z)=\Lambda(z)U(z), \tag{1}$$

where $\Lambda(z)$ is the basic-state ion drag and $U(z)$ the basic-state wind in the x direction. The scale of the horizontal variation of the basic-state wind and ion drag is sufficiently large compared to that of λ that we can neglect this dependence in our analysis. The perturbation ion drag will result in a perturbation horizontal wind $u(x,z)$ so that the total perturbation ion drag $d(x,z)$ is

$$d(x,z)=u(x,z)\Lambda(z)+\lambda(x,z)U(z)+u(x,z)\lambda(x,z). \tag{2}$$

We now obtain the equation for the perturbation horizontal velocity u. Note that if u is sufficiently small, its magnitude will be proportional to the magnitude of $\lambda(x,z)$; and if λ is not too large, we can neglect the last term in (2). Likewise, we can neglect nonlinear terms in the conservation of momentum equation for u. The validity of the linearization can only be established *a posteriori* for a given example. The linearized momentum conservation equation for u is now written as

$$\rho\left(\frac{\partial u}{\partial t}+U\frac{\partial u}{\partial x}+\Lambda u+g\frac{\partial h}{\partial x}\right) - \frac{1}{H}\frac{\partial}{\partial z}\frac{\mu}{H}\frac{\partial u}{\partial z}-\mu\frac{\partial^2 u}{\partial x^2}=-\rho\lambda U, \tag{3}$$

where g is a constant value of gravity; h the perturbation geopotential height; $z=\log(p_0/p)$, where p is pressure and p_0 some reference pressure; μ is the coefficient of viscosity; H the atmospheric scale height; $\rho=p_0e^{-z}/(gH)$ is the basic-state density; and t is time. Coriolis and transverse ion drag terms are assumed to be of lesser importance than the drag in the direction of flow at F layer heights and have been neglected to avoid the necessity of calculating the other component of horizontal motion. To obtain a closed system of equations, we relate perturbation temperature T to h by the hydrostatic law

$$RT=g\frac{\partial h}{\partial z}. \tag{4}$$

We obtain the vertical motion, $w=dz/dt$, from u by continuity, i.e.,

$$\frac{\partial w}{\partial z}-w=-\frac{\partial u}{\partial x}, \tag{5}$$

and couple w to T by the linearized thermodynamic equation

$$\rho C_p\left(\frac{\partial T}{\partial t}+U\frac{\partial T}{\partial x}\right)+pw-\frac{1}{H}\frac{\partial}{\partial z}\frac{k}{H}\frac{\partial T}{\partial z}-k\frac{\partial^2 T}{\partial x^2}=Q. \tag{6}$$

In Eq. (6) Q is the rate of heat input, C_p the specific heat at constant pressure, and k the coefficient of thermal diffusion. The term $pw=-dp/dt$ gives the cooling by adiabatic expansion. The system (3)–(6) is equivalent to that considered by Roble and Dickinson

(1970), except that the assumption of a background wind $U(z)$ has introduced the source of momentum $-\lambda U$ and a momentum transport $U\,\partial u/\partial x$ in the momentum equation, and the temperature transport term $U\,\partial T/\partial x$ in the thermodynamic equation. For a given U, the transport terms will be unimportant provided the horizontal scale of the circulation L is sufficiently large. For the sake of simplicity and since it is our purpose here to explore the consequences of the term $-\lambda U$, we shall assume a horizontal scale large enough that the momentum and temperature transport terms can be neglected. For scales on which the advection terms would be of importance, we shall see that the momentum source $-\lambda U$ excites almost negligible winds and temperatures. Scaling arguments show that inclusion of the transport term for these scales does not change the order of magnitude of the calculated amplitudes.

3. Nondimensionalization

The response of our system is most readily investigated through the use of nondimensional equations. We use carets to denote nondimensional variables, and assume all dimensional variables are proportional to U_0, the order of magnitude of $U(z)$. We take

$$\left.\begin{aligned} u &= U_0\hat{u} \\ w &= (U_0/L)\hat{w} \\ T &= T_c\hat{T} \\ h &= (RT_c/g)\hat{h} \end{aligned}\right\}, \tag{7}$$

where L is the horizontal scale of the motions, $T_c=p_0H_0^2U_0/(Lk_0)$ is a parameter with dimensions of temperature, H_0 is a mean scale height, and μ_0 and k_0 are used for mean coefficients of viscosity and conduction. Following Dickinson (1969), we choose the reference pressure p so that for $p=p_0$ all coefficients of the governing equations are of order unity, where

$$p_0=(L/H_0^2)(gH_0\mu_0k_0/R)^{\frac{1}{2}}. \tag{8}$$

Other simplifying assumptions are now made to derive from the dimensional system (3)–(6) the nondimensional system which is solved numerically in this study:

1) Motions are independent of time.

2) The vertically varying parameters—scale height, viscosity and conductivity coefficients—are replaced by their mean values.

3) The transport terms $U\,\partial u/\partial x$ in (3) and $U\,\partial T/\partial x$ in (6) are neglected.

4) No heat sources are present on the perturbation scale.

5) The perturbation ion drag has a Fourier expansion of the form

$$U(z)\lambda(x,z)=U_0\Lambda_0\bar{\lambda}(z)\Big[\sum_{l=1}^{N}A_l\cos(lx/L)\Big], \tag{9}$$

where the perturbation ion drag scale Λ_0 is chosen so that $\bar{\lambda}(z)$, which gives the nondimensional vertical structure of the perturbation ion drag, has a maximum value of unity. The sum of the A_l and hence the above Fourier series at $x=0$ is unity. The expansion (9) as used for the numerical calculations is a discrete approximation to a Fourier integral such that for practical applications it decays to essentially zero for $x\gg L$.

The above assumptions are made to restrict the number of parameters considered in this study, but any of them can be relaxed without greatly increasing the numerical difficulty in solving the model equations. With these assumptions, we can expand the nondimensional dependent variables in the Fourier series

$$\left.\begin{aligned} \hat{u} &= \sum_{l=1}^{N}u_lA_l\cos(lx/L) \\ \begin{bmatrix}\hat{T}\\ \hat{w}\\ \hat{h}\end{bmatrix} &= \sum_{l=1}^{N}\begin{bmatrix}T_l\\ w_l\\ h_l\end{bmatrix}A_l\sin(lx/L) \end{aligned}\right\}, \tag{10}$$

where u_l, T_l, w_l and h_l are z-dependent Fourier components of the dependent variables. We now write the resulting ordinary differential equations in z as

$$\left.\begin{aligned} e^z\left(\frac{d^2u_l}{dz^2}-\epsilon l^2u_l\right)-\bar{\lambda}(z)u_l-lh_l &= -F\bar{\lambda}(z) \\ T_l-\frac{dh_l}{dz} &= 0 \\ \frac{dw_l}{dz}-w_l-lu_l &= 0 \\ e^z\left(\frac{d^2T_l}{dz^2}-\epsilon l^2T_l\right)-w &= 0 \end{aligned}\right\}, \tag{11}$$

where $\epsilon=H_0^2/L^2$, $\bar{\lambda}(z)$ is the nondimensional perturbation ion drag forcing, $F=\Lambda_0/\Lambda_{00}$, and $\bar{\lambda}(z)=\Lambda(z)/\Lambda_{00}$ is the nondimensional basic-state ion drag using $\Lambda_{00}=(g\mu_0/p_0H_0)$. Eq. (11) is readily solved for an unbounded geometry by numerical methods summarized in the Appendix. Boundary conditions require no sources of momentum, heat or mass at large positive z, and they require the solutions to decay to zero for large negative z.

4. Scaling arguments

We shall first present arguments suggesting qualitative relationships between the circulation variables when the source has a sufficiently small horizontal scale. We shall then consider the nature of the response for a source with extremely large horizontal scale. The parameters $\bar{\lambda}(z)$ and F in (11) are both of order

unity provided the basic-state and perturbation ionization concentrations are of the order of observed F2-layer distributions. Hence, for $l=1$ all variables in (11) can initially be considered of order unity.

If $\tilde{\lambda}(z)$ were a constant, (11) would have the solution

$$\left.\begin{aligned} h_l &= F\tilde{\lambda}/l \\ u_l &= w_l = T_l = 0 \end{aligned}\right\}. \tag{12}$$

In other words, the geopotential height contours would adjust themselves to balance the rate of momentum addition so that no perturbation temperature or motion would occur. Since, in general, $\tilde{\lambda}(z)$ is not constant, there must be a circulation. We shall now discuss why this circulation occurs and show that for sufficiently large wavenumber, its amplitude decreases with increasing wavenumber. If the balance $h=F\tilde{\lambda}/l$ were correct, then from (11) we would have

$$\left.\begin{aligned} T_l &= (F/l)d\tilde{\lambda}/dz \\ w_l &= e^z(F/l)(d^3\tilde{\lambda}/dz^3 - \epsilon l^2 d\tilde{\lambda}/dz) \end{aligned}\right\}. \tag{13}$$

For the height field gradient to be balanced against the momentum source, a positive temperature perturbation must occur by hydrostatics where the source increases with altitude, and a negative temperature perturbation must occur where the source decreases with altitude. The conduction of heat initiated by this distribution of temperature is necessarily balanced by adiabatic warming through vertical motions. According to the continuity equation, the vertical motion must be accompanied by horizontal motion; but viscosity and ion drag will act to destroy this horizontal motion. Hence, an additional perturbation in the height field besides that balancing $F\tilde{\lambda}$ is required. That is, h cannot be described exactly by (12), but should be of the form

$$h_l = F\tilde{\lambda}/l + (lu_l/w_l)\mathrm{O}(l^{-3}) \tag{14}$$

Horizontal molecular transport terms are omitted in deriving this expression.

To interpret the above discussion in terms of a nondimensional horizontal scale L_n of the ionization anomaly, we identify L_n^{-1} with the "dominant" wavenumber of the source. Reference to the numerical solutions indicates that the horizontal scale of u is not L_n but some other scale L^* determined by dissipation processes. In other words, $lu_l \sim u/L^*$, so that neglecting horizontal heat conduction, we infer

$$\left.\begin{aligned} \hat{u}/L^* \approx \hat{w} \approx \hat{T} &\approx FL_n \\ \hat{h} &\approx FL_n[1+\mathrm{O}(L_n^2/L^*)] \end{aligned}\right\} \tag{15}$$

for a sufficiently small source.

The limiting case of an extremely large horizontal source scale can be considered as follows. For any vertical variation of the perturbation ion drag $\tilde{\lambda}$, it is clear that the balances expressed by (15) can no longer hold for a large enough source scale. If the horizontal velocity u increases with the source scale L_n according to (15), then for sufficiently large L_n, the loss of perturbation momentum by ion drag must exceed the momentum added by the source. In fact, the magnitude of the horizontal velocity must be limited by the balance between the momentum source and viscous and ion drag. Thus, from (11) in the limit of large L_n, we have

$$u_l = \mathrm{O}(F). \tag{16}$$

It follows for large L_n that

$$w_l \approx T_l \approx lF, \tag{17}$$

so that w and T are proportional to the inverse of the source scale as identified with l. For source scales large enough to make the relationships (16) and (17) approximately valid, the momentum equation is decoupled to a first approximation from the thermodynamic equation. That is, the horizontal velocities that would be produced if the perturbation height field were neglected imply vertical velocities sufficiently small that adiabatic heating cannot generate perturbation pressure forces as large as the assumed forcing. The source scale necessary to obtain this limit depends, in practice, on the strength of the basic-state stratification. Our numerical calculations indicate that this limiting dependence is realized in the thermosphere only for source scales of global extent or greater, that is, for larger scales than were assumed in deriving the model equations.

5. Model parameterization

The following features are of importance in determining the response: 1) magnitude and vertical structure of the basic-state wind, 2) magnitude and horizontal and vertical structure of the ionization anomaly, and 3) magnitude and vertical structure of the basic-state ion drag.

Large-scale winds calculated from the observed density distribution such as obtained by Geisler (1967) can be approximated by a profile of the form

$$U(z) = U_\infty\{1-\exp[-s(z-z_0)]\}, \tag{18}$$

where s is a constant and z_0 the level of the assumed lower boundary at 120 km.

For reasonable values of s, i.e., $s \approx 1$, $U(z) \approx U_\infty$ at F2 layer heights where the ionization is largest and where ionization anomalies are thus relatively effective in accelerating the neutral gas. Hence, the neutral background wind is essentially specified for our calculations by the value of U_∞. The F2 layer ionization can be modeled by specifying the level of the F2 layer peak using a profile with diffusive equilibrium above the peak and a relatively rapid decrease of ionization with decreasing height below the peak. This behavior is

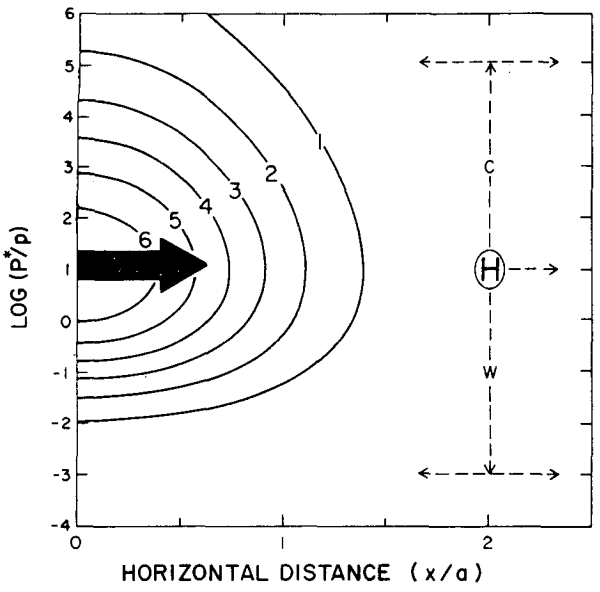

FIG. 1. Rate of momentum addition (cm sec^{-2}) used for the model calculations. The schematic diagram on the right illustrates the atmospheric response to the momentum source, where H indicates the ridge in the pressure surfaces and W and C regions of warming and cooling, respectively.

reproduced adequately by the function

$$N_e(z)=N_{\max}\exp\{-\tfrac{1}{2}(z-z_p)+1-\exp[-\tfrac{1}{2}(z-z_p)]\}, \quad (19)$$

where $N_{\max}$ is the concentration of electrons per unit volume at the F2 layer peak and z_p the level of the F2 layer peak.

Deviations from the basic-state F2 layer ionization can be expected to be roughly proportional to the basic-state ionization concentrations. For this reason, we reduce the number of parameters to be considered by assuming the vertical profile of the perturbation ionization to be the same as the vertical profile of the basic-state ionization. The perturbation ion drag is thus of the form

$$\lambda(x,z)=X(x)\Lambda(z). \quad (20)$$

The horizontal dependence of the ion drag is given by a discrete Fourier series approximation to

$$X(x)=b\exp(-x^2/a^2), \quad (21)$$

where a and b are constants.

The adjustable parameters determining the neutral response in the model calculations are now:

1) The product of the basic-state exospheric wind U_∞ which we equate to U_0, and the perturbation ion drag at the F2 layer peak.

2) The horizontal scale of the perturbation ion drag.

3) The basic-state ion drag at the F2 layer peak.

4) The level of the F2 layer peak in pressure coordinates.

For the following discussion we assume that $U_\infty=200$ m sec^{-1} and there is a maximum ionization anomaly at the F2 layer peak of 5×10^5 electrons cm^{-3}. Since the neutral atmosphere response is linear in the product of these two quantities, all of our numerical results can be readily converted to values appropriate to different background winds and different maximum ionization anomalies.

Almost all of our numerical calculations have been made for $a=0.2L$, $a=L$ and $a=5L$ in Eq. (21), with $L=570$ km. This range of values adequately indicates the variation of the response over scales of interest in the thermosphere. For determining the basic-state ion drag, we have used F2 peak ionization values of 0, N_s and $10N_s$, where $N_s=7.5\times10^5$ electrons cm^{-3}, corresponding, respectively, to very low values of ionization, typical nighttime values, and maximum mid-latitude daytime values observed at times of high solar activity.

The neutral atmosphere is assumed to be isothermal at 1500K and to consist of 75% O and 25% N_2 by volume. The thermal conductivity and viscosity for O is that given by Dalgarno and Smith (1962). We use an identical value for the N_2 viscosity coefficient and one-half the O value for the N_2 conductivity. The value used for the acceleration of gravity g is 870 cm sec^{-2}. Our results, formulated in the pressure coordinate system, are rather insensitive to these details and can be used for a wide range of model atmospheres with negligible differences. With parameter values as described above and the horizontal scale $L=570$ km, the reference pressure in (8) is $p_0=10^{-4}\mu$b. Numerical integrations have been carried out for F2 peaks located one scale height above and one scale height below p_0; this interval corresponds to typical variations of the F2 layer peak level from nighttime to daytime.

In the absence of horizontal diffusion of heat and momentum, the following useful principle can be derived from the perturbation equations. Displacing the basic-state ion drag and momentum source peaks, with preservation of shape, to another pressure level at a fraction P^{-1} of their original pressure is "similar" in the governing equations to increasing the source width by a factor P, as indicated by the definition (8) relating reference pressure to reference scale length. The change of the displacement between the reference level and the ionospheric peak is the same for both cases. For a given source width and peak level, the solutions are then similar in the following sense. If the response with a given source and the peak displaced vertically by an amount $\Delta z=\log P$ is (u, w, h, T), then the response with the given peak level and the source increased in width by the factor P is (Pu, w, Ph, PT). This similarity principle can be used to extend the results of the numerical integrations to other F2 layer peak levels and source scales, provided the source scales are large enough (several hundred kilometers or more)

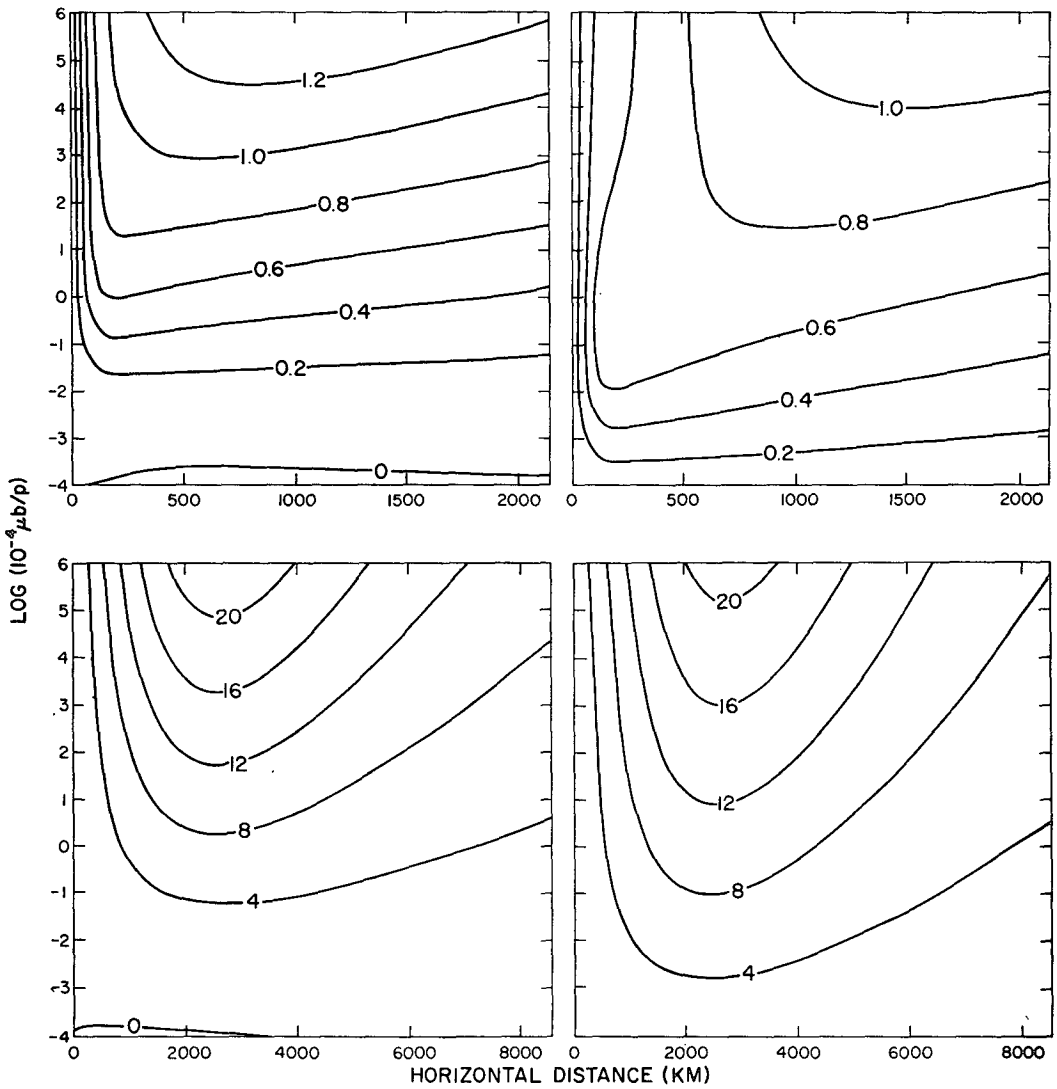

FIG. 2. Perturbation geopotential height contours (km) of constant pressure surfaces for the four cases: a, small-scale, high F2 layer (upper left); b, small-scale, low F2 layer (upper right); c, large-scale, high F2 layer (lower left); and, d, large-scale, low F2 layer (lower right).

to make horizontal diffusion of heat and momentum unimportant.

6. Nature of the response from numerical integrations

The perturbation variable response can be understood schematically as indicated in Fig. 1. Momentum addition pushes the geopotential height surfaces to maximum values at the level of and on the edge of the momentum source. The gradients of the height surface on the far side of the ridge in the height field force the atmosphere in the same direction as the momentum source, and on the near side of the ridge in the opposite direction of the source. At the level of the source region and on the far side of the ridge, there is a net force and thus horizontal motion in the direction of the source. Above and below the source on the near side of the ridge, a return flow is forced except where viscous coupling with the source region is large enough to drag these levels in the direction of the source. Below the source region, the increase of the height field from zero to its maximum value must, according to the hydrostatic equation, produce a positive temperature anomaly. If the height field above the source does not deviate greatly from that required to balance the momentum source, the height gradient must decrease above the center of the maximum source values, thus implying a negative temperature anomaly above the source. Such a negative temperature region occurs only in one of the examples to be discussed. There must be a vertical motion related to the horizontal motions by

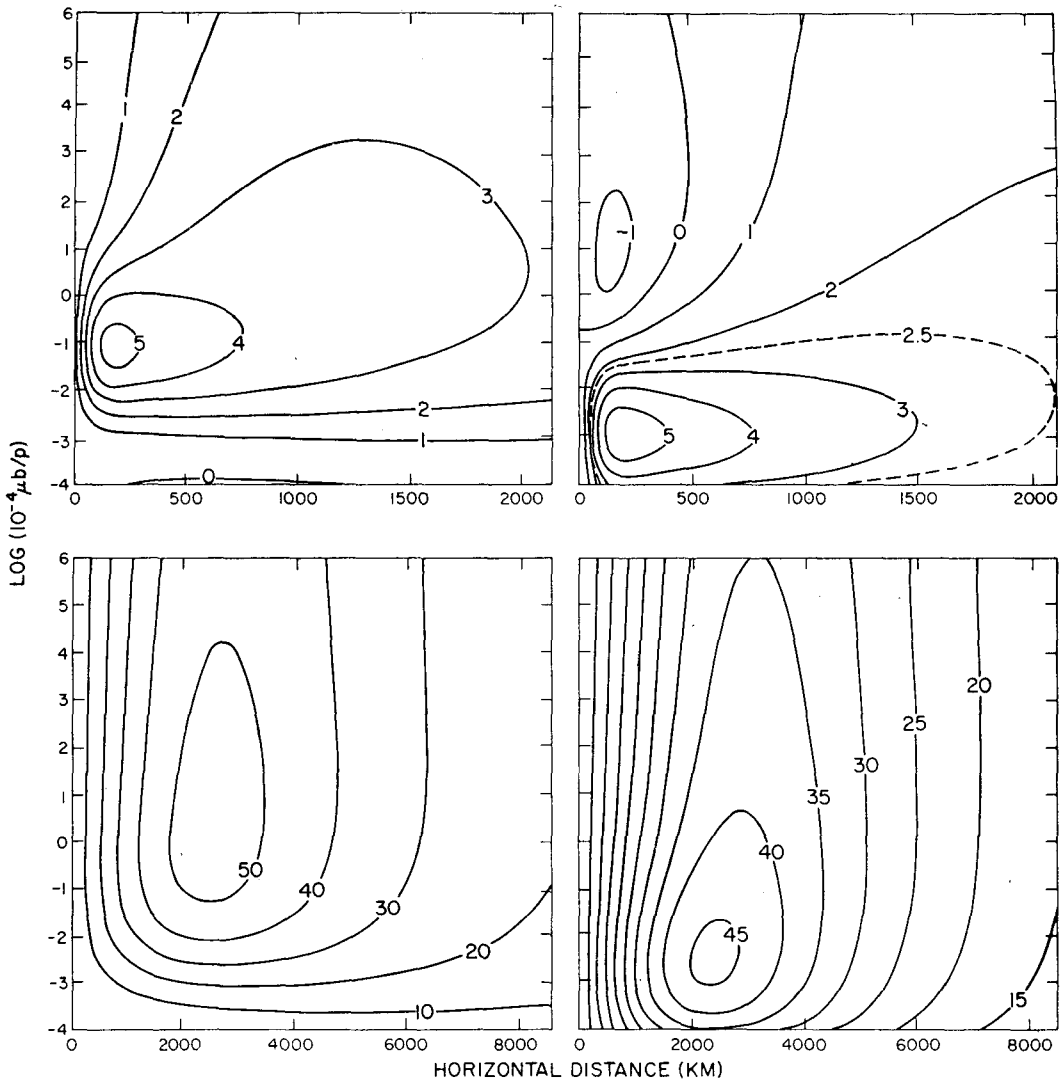

FIG. 3. Perturbation temperature contours (°K) for the four cases as defined in the legend to Fig. 2.

the continuity equation; the vertical motion generates a distribution of adiabatic heating and cooling to balance heat conduction derived from the temperature profile. This requires upward flow above the source and downward flow below the source, with maximum values of vertical motion along the ridge line.

We have carried out a large number of numerical integrations of the dynamic model to understand more fully (in terms of this schematic picture and the previously discussed scaling arguments) how the solutions depend on the horizontal scale of the source, the pressure level of the F2 layer peak, and the magnitude of ion drag. In discussing the conclusions derived from these integrations, we compare two-dimensional plots of results for four examples.

The momentum source as modeled in the previous section is shown in Fig. 1. The maximum rate of momentum addition is 7 cm sec^{-2} for $U_\infty = 200$ m sec^{-1} and a maximum ionization anomaly of 5×10^5 ions cm^{-3}. The other parameters describing the momentum source are the level z_p of the source relative to the reference level of $p_0 = 10^{-4}\,\mu$b, and the width of the source relative to the reference width of $L = 570$ km.

The four cases presented here are

$$\left.\begin{array}{l} \text{a: } z_p = 1,\ N_{\max} = N_s,\ a = 0.2L \\ \text{b: } z_p = -1,\ N_{\max} = 10N_s,\ a = 0.2L \\ \text{c: } z_p = 1,\ N_{\max} = N_s,\ a = 5L \\ \text{d: } z_p = -1,\ N_{\max} = 10N_s,\ a = 5L \end{array}\right\},$$

where N_s is defined as 7.5×10^5 cm^{-3}. The numerical values assumed for these examples are loosely interpreted as follows: $z_p = 1$, high F2 layer; $z_p = -1$, low F2 layer; $N_{\max} = N_s$, typical nighttime F2 layer; $N_{\max} = 10N_s$, maximum observed values for daytime F2 layer; $a = 0.2L = 114$ km, small-scale anomaly; $a = 5L = 2850$ km, large-scale anomaly.

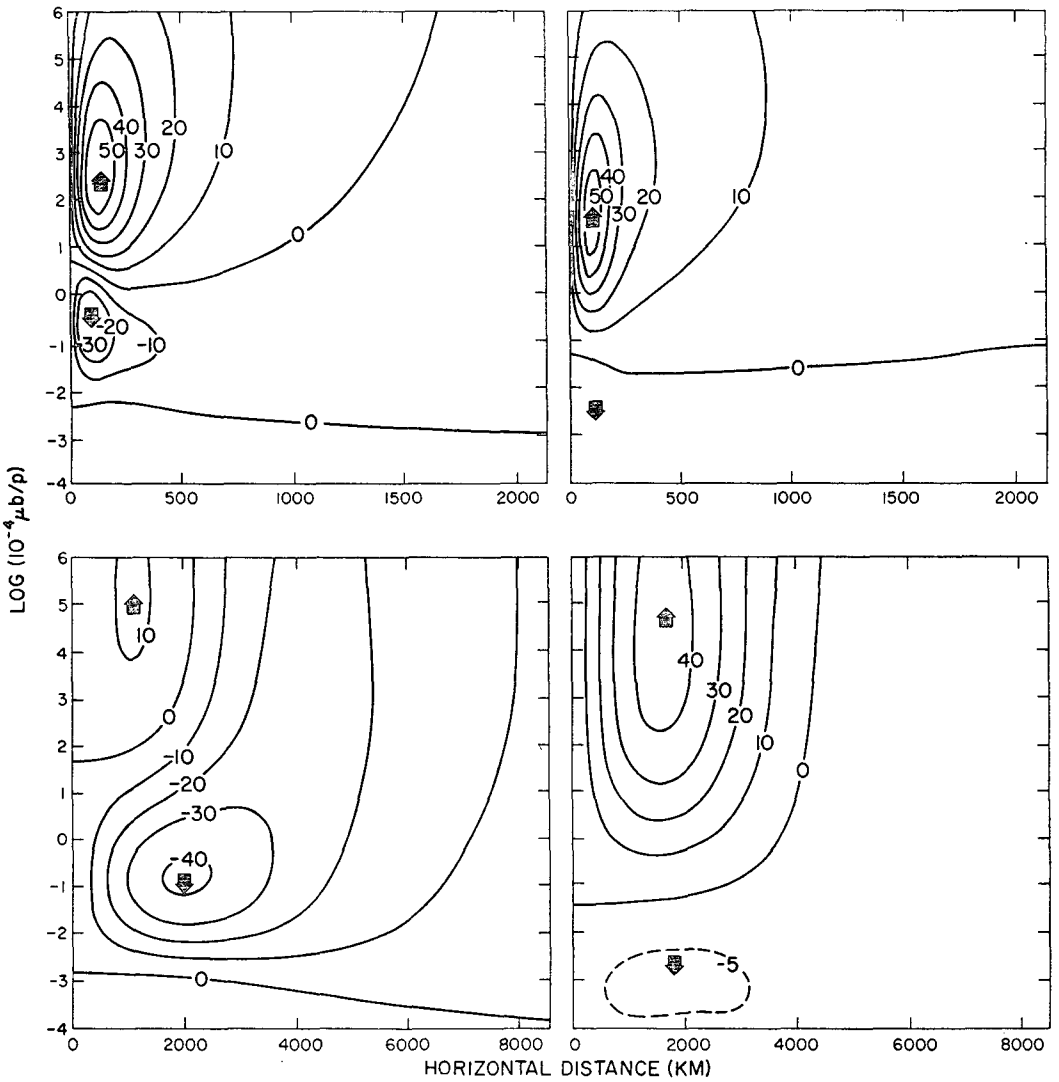

FIG. 4. Vertical motion contours (cm sec^{-1}) for the four cases as defined in the legend to Fig. 2.

According to the similarity principle described in Section 5, in the absence of horizontal diffusion of heat and momentum, the response (u, w, h, T) to a source of scale a and ionospheric peak at $z_p=1$ implies a similar response (e^2u, w, e^2h, e^2T) to a source of horizontal scale (ae^2) and ionospheric peak at $z_p=-1$. Thus, from the response to forcing by the $5L$ scale source at $z_p=1$ (case c), we can infer the response to a 21,000-km scale source at $z_p=-1$; and from the response to the $5L$ scale source at $z_p=-1$ (case d), we can infer the response to a 386-km source at $z_p=1$. The similarity principle is less useful for interpreting results for cases a and b because of the importance of horizontal conduction and horizontal viscous momentum transfer.[2]

Figs. 2–5 show, respectively, the geopotential height, the temperature, and the vertical and horizontal velocities for the examples considered. From these and a number of further numerical integrations summarized in Table 1, we infer the following properties of the response. The height, temperature, and horizontal wind magnitudes in response to the large-scale sources c and d are an order of magnitude larger than the response of these variables to the small-scale sources a and b. The amplitudes of h and T are essentially linear in the source scale for the small-scale sources.

For vertical motion to be linear in the source scale, as predicted by the scaling arguments, it is necessary for the approximate balance between source and height field to be differentiated three times. The departures

[2] *Note added in proof:* The source scale was varied for the numerical calculations by varying the Fourier coefficients in (9) rather than L. The effective scale of Fourier components with wavelengths large compared to the source width did not vary as much as L so the magnitude of u, which is sensitive to the large wavelengths, did not vary as much as if the source shape were exactly preserved.

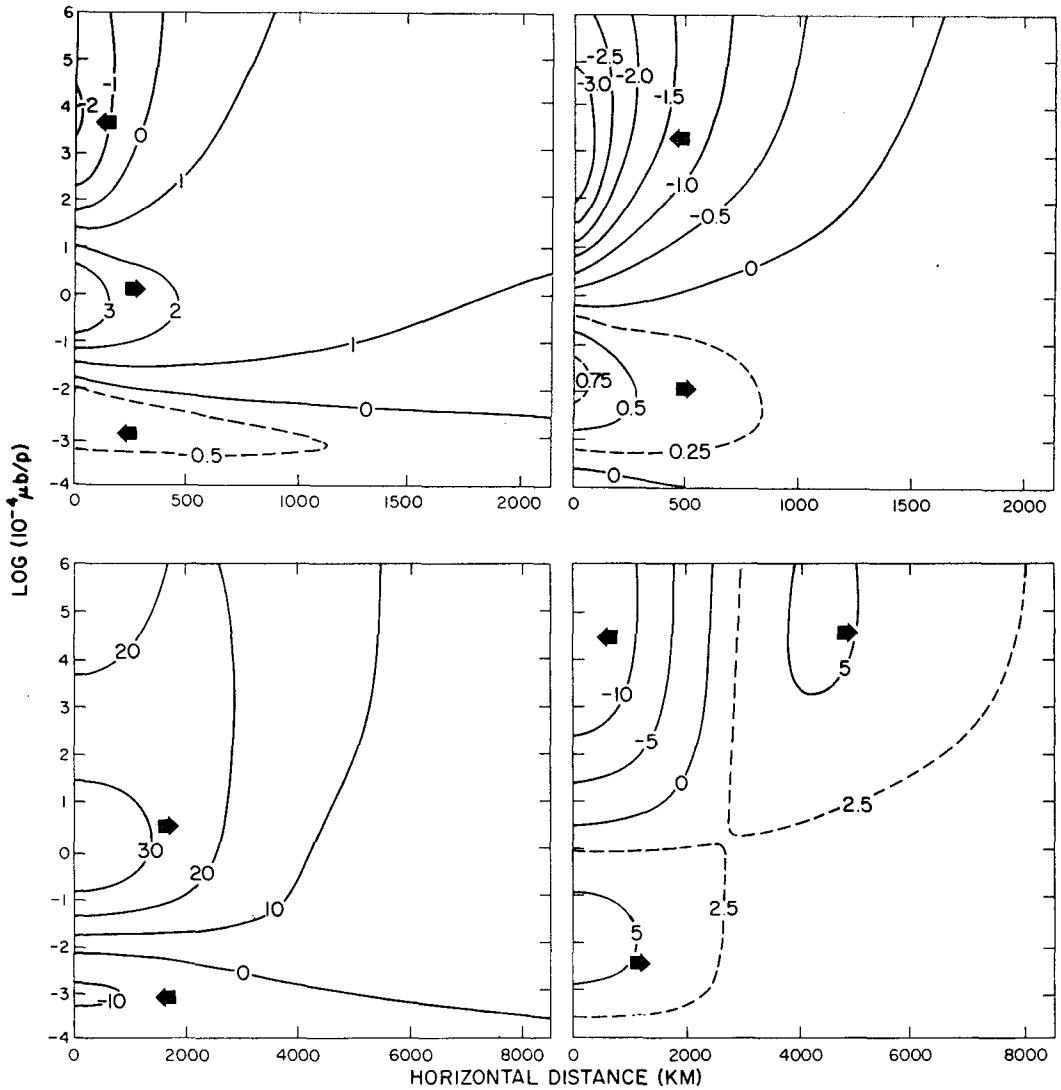

FIG. 5. Horizontal motion contours (m sec^{-1}) for the four cases as defined in the legend to Fig. 2.

from this balance appear to control the magnitude of w down to a scale of O(100 km), where horizontal conduction starts to become important in the thermodynamic equation. We see in Fig. 4 that downward motion below the source level only increases slightly with increasing scale, but is inversely proportional to the pressure of the source level as required by the scaling arguments, i.e., Eq. (13). The upward motions above the source level appear to be determined more by the requirements of continuity than heat balance, and there is no simple dependence on source scale or level in this region.

The maximum amplitudes of the height field as seen in Fig. 2 and the maximum temperature below the source in Fig. 3 are rather insensitive to the level of the source and the magnitude of ion drag over the range of values considered. The maximum temperatures for $a=0.2L$, $z_p=-1$, decreased by $\sim 16\%$ in going from no ion drag to the large values assumed for case b. The sensitivity of the temperature maximum to the value of ion drag increases with increasing z_p and source scale. The maximum T would be doubled in case d if ion drag were omitted; it would be halved if z_p were moved up to $+1$.

The value of ion drag can only influence temperature indirectly through its control of the motions. The decreasing sensitivity to ion drag with decreasing source scale and lowering of source level is easily interpreted according to the scaling arguments of the previous section. That is, as the source scale decreases or the source is lowered, the balance between the height gradients and the source becomes closer, since relatively less height gradient is used to drive horizontal velocities. When this balance is exact, the ion drag cannot have any effect on the temperature. We see in Figs. 2 and 3 that only for case b, the lowest small-

scale source, is the balance above the source center between height gradient and momentum sources sufficiently close that the height decreases with decreasing pressures, requiring a negative temperature region to be present. For the other examples shown, the viscous drag above the source is sufficiently great to prevent this degree of balance.

For the small-scale sources, the horizontal velocities also change only slowly as ion drag is increased, due to the balances discussed above. For example, u decreases by a factor of 2 if the ion drag is increased by a factor of 10 in case a. This small decrease of u with large ion drag increase is partly due to the decrease of the positive height gradient as ion drag increases and partly due to the decrease of viscous drag. In the limit of small source scale, the values of u are determined largely from vertical motion by the requirements of continuity. The height gradients then adjust to balance the u-dependent terms in the equation of motion. On the other hand, for large enough scales not much adjustment of the height is possible. The amplitude of u for a large enough source scale becomes inversely proportional to the total drag exerted on u. In case d, without ion drag, the horizontal velocity would be an order of magnitude greater.

In case c, the horizontal flow forced by the source exerts viscous drag on the levels above the source. In the other examples shown in Fig. 5, the positive height gradient drives return flows above the source. Return flows of relatively small velocity but large mass flux occur below the source, as seen also in Fig. 5. The return flow in d is below the plotted region.

For large enough scales, the velocity amplitude is controlled by balance between drag terms and the momentum source, while u has the scale of the source; hence, w, T and h should decrease with further increase of length scale. Table 2 lists the approximate scales beyond which these parameters start to decrease with increasing u.

TABLE 1. Maximum amplitudes of the perturbation variables for sources of the three assumed length scales a, of the two assumed values of the ionospheric peak z_p, and of the three assumed maximum concentrations of ionization N_{max} for $L=570$ km and $N_s=7.5\times10^5$ cm^{-3}. The variables are the maximum positive temperature perturbation; w, the maximum downward vertical velocity; and u, the maximum horizontal velocity in the direction of the applied momentum source.

a (km)	z_p	N_{max}	u (m sec^{-1})	w (cm sec^{-1})	T (°K)
0.2L	1	0	5.7	−37	5.6
0.2L	1	N_s	4.0	−36	5.4
0.2L	1	$10N_s$	1.8	−12	4.6
0.2L	−1	0	4.2	− 8	6.6
0.2L	−1	$10N_s$	0.8	− 7	5.7
L	1	0	21.4	−42	21.5
L	1	N_s	13.4	−37	19.4
L	1	$10N_s$	4.5	−21	13.5
L	−1	$10N_s$	2.7	− 8	19.6
5L	1	0	72.1	−59	75.2
5L	1	N_s	36.3	−42	54.1
5L	1	$10N_s$	8.5	−15	23.7
5L	−1	0	58.0	−36	92.2
5L	−1	$10N_s$	5.9	− 8	46.2

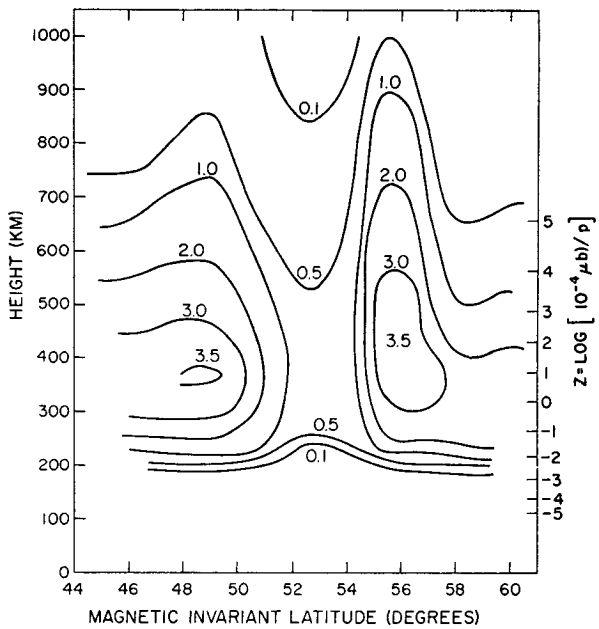

FIG. 6. Electron density (10^5 electrons cm^{-3}) measured in the vicinity of the 28–29 September 1967 stable auroral red arc.

7. Observed ionization anomalies

A global morphology of the topside ionosphere shows many large-scale electron density anomalies (e.g., Thomas *et al.*, 1966; Nelms, 1966; Chan and Colin, 1969; Warren, 1969). These deviations occur on various space and time scales (Rishbeth, 1968). A few of the more persistent spatial anomalies are discussed below to indicate the application of the theory developed in this paper.

a. Electron density depression within a stable auroral red arc

An electron density depression within the stable auroral red arc has been observed as a common feature of all the arcs examined thus far (King and Roach, 1961; Clark *et al.*, 1969; Norton and Marovich, 1969; Roble *et al.*, 1970, 1971; Chandra *et al.*, 1971). The red

TABLE 2. Length scale for which maximum temperature and vertical motion perturbations are obtained for given strength source at $z_p=1$ for $N_s=7.5\times10^5$ cm^{-3}.

N_{max}	Length scale (km)
0	10^4
N_s	5×10^3
$10N_s$	2×10^3
10^3N_s	200

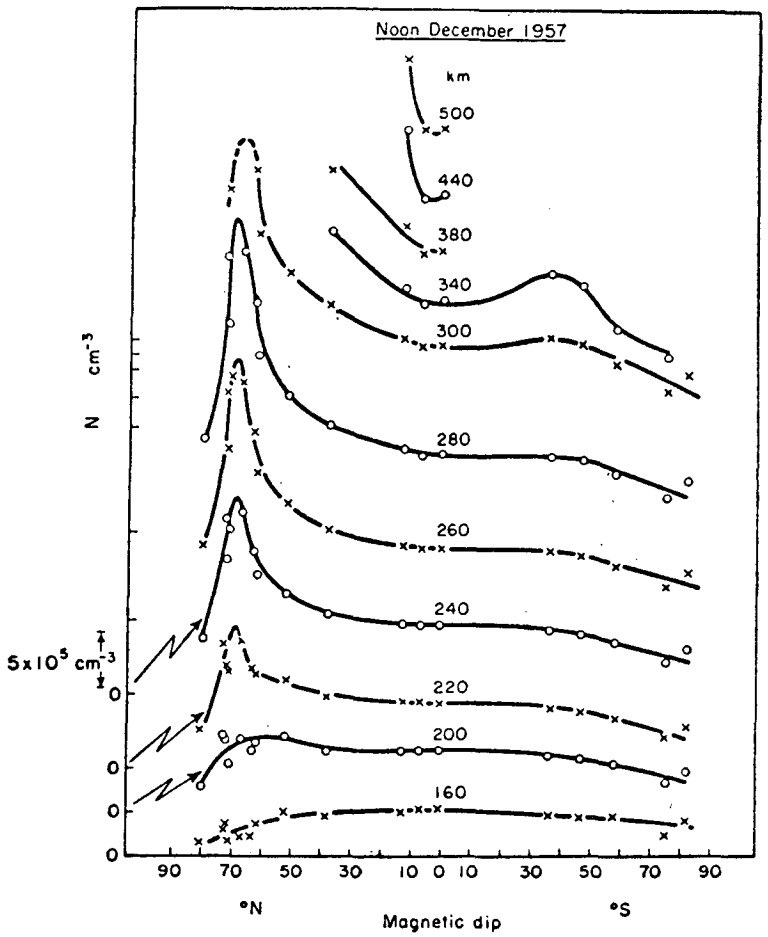

FIG. 7. Variation with magnetic dip of the mean quiet electron density N at a series of fixed heights in the F region at local noon on December 1957. The zero of the scale for the electron density at each height is marked (Croom *et al.*, 1959).

arcs and the electron density depression lie along constant magnetic invariant latitudes and extend in longitude at least around the nightside of the earth. The red arcs are persistent and stable with a lifetime of the order of 10 hr or longer (Roach and Roach, 1963; Nagy *et al.*, 1970). Although no direct observations have been made of the lifetime of the electron density depression, the close association between the red arcs and the depression indicate that the two probably have comparable lifetimes. An electron density depression determined from data from the Alouette 2 satellite as it passed over the 28–29 September 1967 red arc is shown in Fig. 6. The depression occurred within the red arc down to at least the bottom of the sounding at the F2 layer peak. The north-south horizontal scale is approximately 200 km. The electron density at the center of the depression is an order of magnitude less than the surrounding region outside the arc. Several other red arcs have been examined by Roble *et al.* (1971). They show that an electron density depression existed within the 31 October–1 November 1968 red arc at the same time that Hays and Roble (1971) measured a neutral wind of the order of 250–300 m sec^{-1} in the vicinity of the red arc.

b. Longitudinally aligned electron density enhancement

Da Rosa and Waldman (1970) have observed an ionization enhancement in mid-latitudes of approximately the same size as the depression within the red arc. The anomaly persisted during the day and was aligned along a geomagnetic meridian. The horizontal scale was approximately 1° in longitude and 20° in latitude, while the total density varied approximately 25% from the mean ionization background.

c. Mid-latitude electron density trough

Muldrew (1965) has discussed the high and mid-latitude F region electron density troughs. The troughs are aligned in the magnetic east-west direction with a horizontal scale ~5–10° in latitude. The trough exists in the topside ionosphere down at least to the F2 layer

peak (Miller, 1970). The movements of the trough are related to time and the geomagnetic index K_p. They also appear to be related to the plasmapause position (Rycroft and Burnell, 1970; Carpenter, 1971). The troughs are semi-permanent features. The electron density in the topside ionosphere may vary by an order of magnitude in a latitudinal distance of 10° (Chan and Colin, 1969). The nighttime diurnal winds, which are primarily northerly, will interact with this mid-latitude electron density trough and thus produce a momentum source for the neutral gas as described in this paper.

d. Ionization anomalies during geomagnetic storms

Sato (1968) and Warren (1969) have shown that the topside ionosphere is greatly disturbed during geomagnetic storms and contains persistent ionization anomalies of various scales. These anomalies occur at various latitudes from equatorial to polar regions. Power and Rush (1968) have discussed an ionization enhancement in polar regions over the mean mid-latitude electron density. The electron density in polar regions often exceeds the equatorial electron density at the same latitude. Croom *et al.* (1959) have described a maximum in the electron density above 200 km in the form of a narrow ridge centered on a dip angle of 70N which extends 10° to either side of the ridge (Fig. 7). The anomaly was observed during the month of December 1957 during a time of extremely high solar activity (sunspot number around 200). This feature is not observed when the sunspot number is less than ~100. Anomalies that occur during geomagnetically disturbed conditions thus act as further momentum sources for the neutral atmosphere on a less-than-global scale by interacting with the global-scale wind system.

e. Sunrise-sunset electron density variations

A large change in the electron density occurs during sunrise and sunset (Thomas, 1962; Evans, 1968). The electron density change extends vertically throughout the ionosphere and the densities change by an order of magnitude in 1–2 hr (or 15–30° longitude, assuming time is interchangeable with longitude). The average daily variation of the plasma frequency for November 1964, as determined by the Millstone Hill ionospheric radar, is shown in Fig. 8 (Evans, 1967). The electron density is related to the plasma frequency by $n_e = 1.24 \times 10^4 f_N^2$ where n_e is the electron density (cm^{-3}) and f_N is the plasma frequency (MHz). The day-night electron density variation results in a large horizontal-scale departure from the global mean ionization. The interaction of this ionization anomaly with the global-scale wind system produces a large horizontal-scale momentum source. The consequent large perturbation in the gradient of the horizontal flow at dawn and dusk which are obtained through calculations such as those of Geisler (1967) will be reduced, but not entirely removed by the perturbation pressures determined by coupling with the thermodynamics.

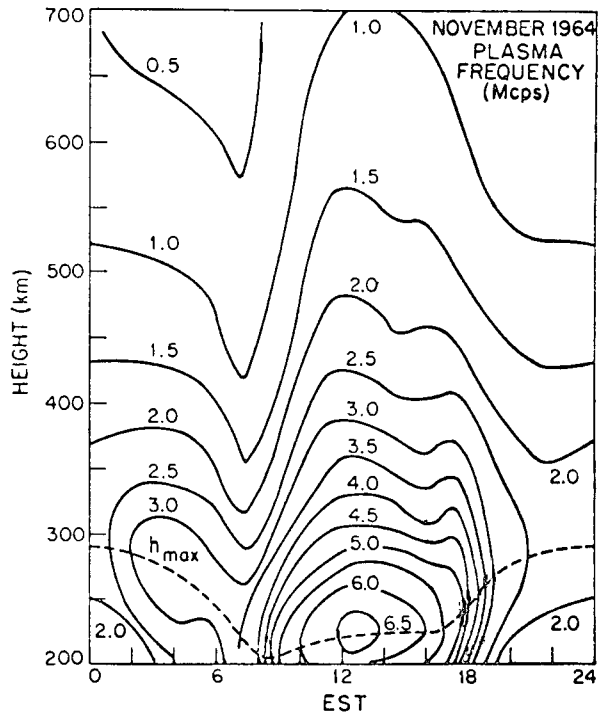

FIG. 8. Diurnal variation of plasma frequency f_N for November 1964 over Millstone Hill (Evans, 1967).

8. Conclusions

The response of the neutral thermosphere to the local momentum source inferred from a spatial anomaly in the ion drag is primarily determined by the magnitude of the basic-state wind and the magnitude and horizontal scale of the ionization anomaly. The detailed structure of the response is determined to a lesser extent by the magnitude and vertical structure of the basic-state ionization and by the vertical structure of the basic-state wind and the ionization anomaly. Several particular applications were discussed. The calculations show that for horizontal scales of the order of a few hundred kilometers, corresponding to the scale of the ionization anomaly within the stable auroral red arc or to the mid-latitude electron density trough, the perturbation temperature and circulation response are insignificant and the mean wind is not greatly disturbed as it flows through the ionization anomaly. On the other hand, for horizontal scales of the order of a few thousand kilometers, corresponding to the scale of the persistent ionization anomalies observed during geomagnetic disturbed periods or in the day-night electron density variation at sunrise or sunset, significant horizontal velocity, vertical motion, and temperature fields will be superimposed upon the basic-state wind.

These conclusions are derived from a two-dimensional

steady-state dynamic model of the neutral thermosphere. They are applicable to the persistent F2 layer electron anomalies, but not to transient phenomena with time scales of a few hours or less.

Our results support the contention that smooth global-scale distributions of ion drag can be used with little error in developing models of thermospheric dynamics. On the other hand, the use of global-mean ion drag by itself is inadequate for such models. Inclusion of global-scale variations in the ion drag should lead to quantitatively different conclusions regarding the thermospheric winds and temperature oscillations.

APPENDIX

Numerical Solutions

For each Fourier component, we need to solve the system of equations (11). We have included in our numerical solution a radiative damping term and a heating term which were set equal to zero for the present calculations. We also allow a nondimensional static stability $S(z)$ that was assumed to be unity for the present calculations. The equations considered are

$$\left.\begin{aligned} e^z\left(\frac{d^2u}{dz^2}-\epsilon l^2u\right)-\lambda(z)u-l^2h&=-lF(z)\\ T-\frac{\partial h}{\partial z}&=0\\ \frac{dw}{dz}-w-u&=0\\ e^z\left(\frac{d^2T}{dz^2}-\epsilon l^2T\right)-a(z)T-wS(z)&=-Q(z)\end{aligned}\right\}. \quad \text{(A1)}$$

We have dropped l subscripts from (11) and used $u=lu_l$. Here $F(z)$ and $Q(z)$ represent the lth Fourier components of given momentum and heat sources, respectively, and $a(z)T$ is a radiative damping term that is assumed to be linear in the perturbation temperature.

For simplicity, let

$$\left.\begin{aligned}\lambda(z)+\epsilon l^2e^z&=f(z)\\ a(z)+\epsilon l^2e^z&=c(z)\end{aligned}\right\}.$$

We make the change of variables

$$\left.\begin{aligned}\varphi&=e^{-z/2}w\\ \psi&=-e^{z/2}\frac{\partial u}{\partial z}+f\frac{\varphi}{2}\end{aligned}\right\}, \quad \text{(A2)}$$

which allows (A.1) to be written as

$$\frac{d^2y}{dz^2}=Gy-g, \quad \text{(A3)}$$

where

$$y=\begin{bmatrix}T\\ \varphi\\ \psi\end{bmatrix},$$

$$G=\begin{bmatrix}ce^{-z} & Se^{-z/2} & 0\\ 0 & \frac{1}{2}(\frac{1}{2}+e^{-z}f) & -e^{-z}\\ -l^2e^{-z/2} & \frac{1}{2}\left(f''+f'-\frac{f^2}{2}e^{-z}\right) & \frac{1}{2}(\frac{1}{2}+fe^{-z})\end{bmatrix},$$

where the primes denote differentiation with respect to z, and

$$g=\begin{bmatrix}e^{-z}Q(z)\\ 0\\ -e^{-z/2}lF(z)\end{bmatrix}.$$

The top boundary conditions assumed are

$$\left.\begin{aligned}\frac{\partial u}{\partial z}+\epsilon^{\frac{1}{2}}lu&=0\\ \frac{\partial T}{\partial z}+\epsilon^{\frac{1}{2}}lT&=0\\ e^{-z}w&=0\end{aligned}\right\}, \quad \text{for } \lim_{z\to\infty}. \quad \text{(A4)}$$

We translate these to some finite level by obtaining the three power series solutions to (A.3) in the variable $\zeta=e^{-z}$ about the singular point $\zeta=0$ which satisfy (A.4).

The bottom boundary condition assumed is

$$\lim_{z\to-\infty} y(z)=0. \quad \text{(A5)}$$

This is translated to a finite level using a WKB asymptotic solution to (A.3) that satisfies (A.5).

Fourth-order differencing is used to approximate (A.3) between a top level of $z=7$ and a bottom level of $z=-10$ by a block tridiagonal matrix. Twenty grid points per scale height were used. The Green function solution obtained by Dickinson (1969) was evaluated numerically for certain simple forcing functions. The present numerical solution was in accord with the analytic solutions to six digits of accuracy. About 5 sec on the Control Data Corporation 6600 computer are required for one such numerical integration using the standard Gaussian elimination technique.

Acknowledgments. We wish to thank Dr. R. B. Norton for valuable discussions on ionization anomalies.

REFERENCES

Carpenter, D. L., 1971: OGO-2 and 4 VLF observations of the asymmetric plasmapause near the time of SAR-ARC events. (Submitted to *J. Geophys. Res.*)

Chan, K. L., and L. Colin, 1969: Global electron density distributions from topside soundings. *Proc. IEEE*, **57**, 990–1004.

Chandra, S., E. J. Maier, B. E. Troy and B. C. Narasinga Rao, 1971: Subauroral red arcs and associated ionospheric phenomena. *J. Geophys. Res.*, **76**, 920–925.

Clark, W. L., J. R. McAfee, R. B. Norton and J. M. Warnoch, 1969: Radio wave reflections from large horizontal gradients in the topside ionosphere. *Proc. IEEE*, **57**, 493–496.

Croom, S., A. Robbins and J. O. Thomas, 1959: Two anomalies in the behavior of the F2 layer of the ionosphere. *Nature*, **184**, 2003–2004.

Da Rosa, A. V., and H. Waldman, 1970: Evidence for persistent longitudinal anomalies in the ionospheric electron content. *J. Geophys. Res.*, **75**, 7276–7279.

Dalgarno, A., and F. J. Smith, 1962: The thermal conductivity and viscosity of atomic oxygen. *Planetary Space Sci.*, **9**, 1–2.

Dickinson, R. E., 1969: The steady circulation of a nonrotating, viscous, heat-conducting atmosphere. *J. Atmos. Sci.*, **26**, 1191–1198.

Evans, J. V., 1967: Midlatitude F region densities and temperatures at sunspot minimum. *Planetary Space Sci.*, **15**, 1387–1405.

——, 1968: Sunrise behavior of the F layer at midlatitudes. *J. Geophys. Res.*, **73**, 3489–3504.

Geisler, J. E., 1967: A numerical study of the wind system in the middle thermosphere. *J. Atmos. Terr. Phys.*, **29**, 1469–1482.

Hays, P. B., and R. G. Roble, 1971: Direct observations of thermospheric winds during geomagnetic storms. *J. Geophys. Res.*, **76**, 5316–5321.

King, G. A. M., and F. E. Roach, 1961: Relationship between red auroral arcs and ionospheric recombination. *J. Res. NBS*, **65D**, 129–135.

Kohl, H., and J. W. King, 1967: Atmosphere winds between 100 and 700 km and their effect on the ionosphere. *J. Atmos. Terr. Phys.*, **29**, 1045–1062.

Miller, N. J., 1970: The main electron trough during the rising solar cycle. *J. Geophys. Res.*, **75**, 7175–7181.

Muldrew, D. B., 1965: F layer ionization troughs deduced from Alouette data. *J. Geophys. Res.*, **70**, 2635–2650.

Nagy, A. F., R. G. Roble and P. B. Hays, 1970: Stable mid-latitude red arcs: Observations and theory. *Space Sci. Rev.*, **11**, 709–727.

Nelms, G. L., 1966: Seasonal and diurnal variations of the distribution of electron density in the topside of the ionosphere. *Electron Density Profiles in Ionosphere and Exosphere*, New York, North-Holland Publ. Co., 630 pp.

Norton, R. B., and E. Marovich, 1969: Alouette observations taken during a middle-latitude red arc. *Proc. IEEE*, **57**, 1158–1160.

Power, C. F., and C. M. Rush, 1968: The ionization maximum in polar latitudes. *Ionospheric Radio Communications*, New York, Plenum, 459 pp.

Rishbeth, H., 1968: On explaining the behavior of the ionospheric F region. *Rev. Geophys.*, **6**, 33–72.

Roach, F. E., and J. R. Roach, 1963: Stable 6300 Å auroral arcs in mid-latitudes. *Planetary Space Sci.*, **11**, 532–545.

Roble, R. G., and R. E. Dickinson, 1970: Atmospheric response to heating within a stable auroral red arc. *Planetary Space Sci.*, **18**, 1489–1498.

——, P. B. Hays, and A. F. Nagy, 1970: A comparison between calculated and observed features of a stable mid-latitude red arc. *J. Geophys. Res.*, **75**, 4261–4265.

——, R. B. Norton, J. A. Findlay and E. Marovich, 1971: The calculated and observed features of several stable auroral red arcs. *J. Geophys. Res.* (in press).

Rycroft, M. J., and S. J. Burnell, 1970: Statistical analysis of movements of the ionospheric trough and the plasmapause. *J. Geophys. Res.*, **75**, 5600–5604.

Sato, T., 1968: Electron density variations in the topside ionosphere between 60°N and 60°S geomagnetic latitude associated with geomagnetic disturbances. *J. Geophys. Res.*, **73**, 6225–6241.

Thomas, J. O., 1962: The electron density distributions in the F-region of the ionosphere. *Electron Density Profiles*, New York, Pergamon Press, 418 pp.

Thomas, J. O., M. J. Rycroft, L. Colin and K. L. Chan, 1966: The topside ionosphere. Proc. NATO Advanced Study Institute. *Electron Density Profiles in Ionosphere and Exosphere*, New York, North-Holland Publ. Co., 630 pp.

Warren, E. S., 1969: The topside ionosphere during geomagnetic storms. *Proc. IEEE*, **57**, 1029–1036.